

Compton scattering near threshold

Max Kircher,¹ Florian Trinter,^{2,3} Sven Grundmann,¹ Isabel Vela-Perez,¹ Simon Brennecke,⁴ Nicolas Eicke,⁴ Jonas Rist,¹ Sebastian Eckart,¹ Salim Houamer,⁵ Ochbadrakh Chuluunbaatar,^{6,7} Yuri V. Popov,^{8,6} Igor P. Volobuev,⁸ Kai Bagschick,² M. Novella Piancastelli,^{9,10} Manfred Lein,⁴ Till Jahnke,¹ Markus S. Schöffler,¹ and Reinhard Dörner^{1,*}

¹*Institut für Kernphysik, J. W. Goethe Universität,
Max-von-Laue-Str. 1, D-60438 Frankfurt, Germany*

²*FS-PETRA-S, Deutsches Elektronen-Synchrotron DESY, Notkestr. 85, D-22607 Hamburg, Germany*

³*Molecular Physics, Fritz-Haber-Institut der Max-Planck-Gesellschaft, Faradayweg 4-6, D-14195 Berlin, Germany*

⁴*Institut für Theoretische Physik, Leibniz Universität Hannover, Appelstr. 2, D-30167 Hannover, Germany*

⁵*LPQSD, Department of Physics, Faculty of Science, University Sétif-1, 19000, Sétif, Algeria*

⁶*Joint Institute for Nuclear Research, Dubna, Moscow region 141980, Russia*

⁷*Institute of Mathematics, National University of Mongolia, Ulan-Bator, Mongolia*

⁸*Skobel'syn Institute of Nuclear Physics, Lomonosov Moscow State University, Moscow 119991, Russia*

⁹*Sorbonne Universités, CNRS, UMR 7614, Laboratoire de Chimie Physique Matière et Rayonnement, F-75005 Paris, France*

¹⁰*Department of Physics and Astronomy, Uppsala University, P.O. Box 516, SE-751 20 Uppsala, Sweden*

(Dated: May 4, 2020)

Compton scattering is one of the fundamental interaction processes of light with matter. Already upon its discovery [1] it was described as a billiard-type collision of a photon kicking a quasi-free electron. With decreasing photon energy, the maximum possible momentum transfer becomes so small that the corresponding energy falls below the binding energy of the electron. Then ionization by Compton scattering becomes an intriguing quantum phenomenon. Here we report a kinematically complete experiment on Compton scattering at helium atoms below that threshold. We determine the momentum correlations of the electron, the recoiling ion, and the scattered photon in a coincidence experiment finding that electrons are not only emitted in the direction of the momentum transfer, but that there is a second peak of ejection to the backward direction. This finding links Compton scattering to processes as ionization by ultrashort optical pulses [2], electron impact ionization [3, 4], ion impact ionization [5, 6], and neutron scattering [7] where similar momentum patterns occur.

Doubts about energy conservation in Compton scattering on the single-event level were the trigger motivating the invention of coincidence measurement techniques by Bothe and Geiger [8]. This historic experiment settled the dispute on the validity of conservation laws in quantum physics by showing that for each scattered photon there is an electron ejected in coincidence. Surprisingly however, even 95 years after this pioneering work, coincidence experiments on the Compton effect are extremely scarce and they are restricted to solid-state systems [9, 10]. This lack of detailed experiments left further progress in the field of Compton scattering to large extent to theory. Due to missing experimental techniques, much of the poten-

tial of using Compton scattering as a tool in molecular physics remained untapped [11]. The small cross section of 10^{-24} cm² (six orders of magnitude below typical photoabsorption cross sections at the respective thresholds), together with the small collection solid angle of typical photon detectors prohibited coincidence experiments on free atoms and molecules up to now. In the present work, we have solved that problem by using the highly efficient COLd Target Recoil Ion Momentum Spectroscopy (COLTRIMS) technique [12] to detect the electron and the ion momentum in coincidence. The He⁺ ion and electrons with an energy smaller than 25 eV are detected with 4π collection solid angle. The momentum vector of the scattered photon can be obtained using momentum conservation, therefore circumventing the need for a photon detector. This allows us, for the first time, to obtain a kinematically complete data set of ionization by Compton scattering of atoms addressing the intriguing low-energy, near-threshold regime. It has been frequently pointed out in the theoretical literature that such complete measurements of the process – as opposed to detection of the emitted electron or scattered photon only – are the essential key for sensitive testing of theories [13] as well as to allow for a clean physics interpretation of the results [14].

For the case of Compton scattering at a *quasi-free* electron, the angular distribution of the scattered photon is given by the Thomson cross section (see Fig. 1a). A binding of the electron modifies the binary scattering scenario by adding the ion as a third particle. The often invoked impulse approximation accounts for one of the effects of that binding, namely the electron's initial momentum distribution. According to this approximation, the initial electron momentum is added to the momentum balance, while the binding energy is neglected. In this model the ion momentum is defined such that it compensates only for the electron's initial momentum. The impulse approximation works well when the binding energy is negligible compared to the energy of the electron carrying the mo-

* doerner@atom.uni-frankfurt.de

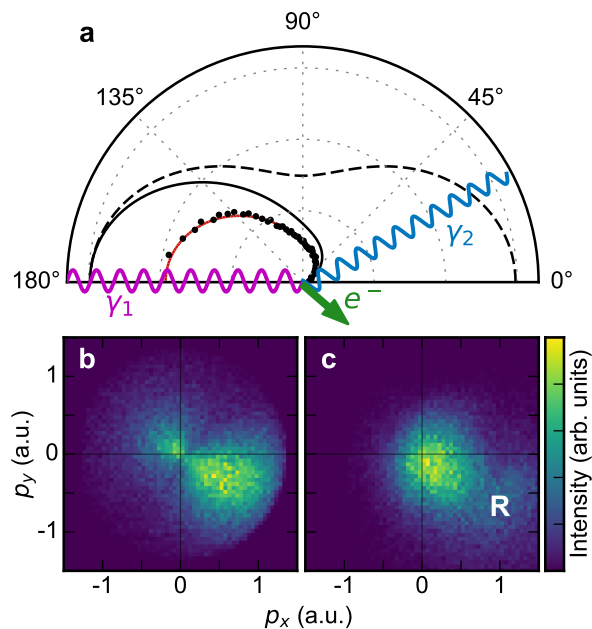


FIG. 1. **Scheme of ionization by Compton scattering at $h\nu = 2.1$ keV.** **a**, The wavy lines indicate the incoming and outgoing photon, the green arrow depicts the momentum vector of the emitted electron. Dashed line: Thomson cross section, i.e. angular distribution of a photon scattering at a free electron. Black dots: experimental photon angular distribution for ionization of He by Compton scattering, integrated over all angles and energies of the emitted electrons below 25 eV. The statistical error is smaller than the dot size. Solid black line: A^2 approximation for all electron energies. Solid red line: A^2 approximation for electron energies below 25 eV. The calculations were done using approach A (see Methods). The solid and dotted lines are multiplied by a factor of 1.9. **b**, Momentum distribution of electrons emitted by Compton scattering of 2.1 keV photons at He. The coordinate frame is the same as in **a**, i.e. the plane is defined by the incoming (horizontal) and scattered photon (upper half plane). The momentum transfer points to the forward lower half plane. The data are integrated over the out-of-plane electron momentum components. **c**, He^+ ion momentum distribution for the same conditions as in **b**. Refer to the main text for an explanation of the feature **R**.

momentum Q transferred by the photon. The maximum value of Q is reached for photon back-scattering, and is twice the photon momentum E_1/c , with E_1 being the incoming photon energy. For helium with a binding energy of 24.6 eV this gives a threshold of $E_1 \approx 2.5$ keV, below which photon back-scattering at an electron at rest does not provide enough energy to overcome the ionization threshold. In the present experiment we use a photon energy $E_1 = 2.1$ keV, well below that threshold. There, the cross section for ionization by Compton scattering has dropped to about 20% of its maximum value of about 10^{-24} cm² [15]. As expected, we observe that the photon scattering angular distribution differs significantly from the Thomson cross section (Fig. 1a). The most striking

difference is that all forward angles of photon emission are suppressed and almost only back-scattered photons lead to ionization. This measured cross section shows excellent agreement with our theoretical model which is described in detail in the Methods section.

What is the mechanism facilitating ionization at these low photon energies and small momentum transfers? Our coincidence experiment can answer this question by providing the momentum vectors of all particles, i.e. the incoming (\mathbf{k}_1) and outgoing photon (\mathbf{k}_2), the electron (\mathbf{p}_e), and the ion (\mathbf{p}_{ion}) for each individual Compton ionization event. This event-by-event momentum correlation gives access to the various particles' momentum distributions in the intrinsic coordinate frame of the process, which is a plane spanned by the wave vectors of the incoming and the scattered photon (Fig. 1). This plane also contains the momentum transfer vector $\mathbf{Q} = \mathbf{k}_1 - \mathbf{k}_2$. In Fig. 1b,c, by definition, the photon is scattered to the upper half plane and the momentum transfer \mathbf{Q} , i.e. the kick by the photon, points forward and into the lower half plane. The electron momentum distribution visualized in this intrinsic coordinate frame shows two distinct islands, one in the direction of the momentum transfer and a second, smaller one, to the backward direction, i.e. opposite to the momentum transfer direction. These two maxima are separated by a minimum. The He^+ ions (Fig. 1c) are also emitted to the forward direction. In addition to a main island close to the origin, there are also ions which are emitted strongly in forward direction towards the region noted by **R** (Recoil) in Fig. 1c. This ion momentum distribution shows strikingly that in the below-threshold regime, the situation is very different from the quasi-free electron scattering considered in the standard high-energy Compton process. In the latter case, the ion is only a passive spectator to the photon-electron interaction and, consequently, the ion momenta are centered at the origin of the coordinate frame employed in Figs. 1b,c [15–18].

The observed bimodal electron momentum distribution becomes even clearer when we examine a subset of the data for which the photon is scattered to a certain direction (Fig. 2). This shows that the momentum distribution follows the direction of momentum transfer and the nodal plane is perpendicular to \mathbf{Q} . Such bimodal distributions are known from different contexts. For example, for ionization by electron impact ($e, 2e$) [4] and ion impact [5], the forward lobe has been termed binary lobe, for obvious reasons, while the backward peak is referred to as recoil peak. The name alludes to the fact that in order for the electron to be emitted opposite to the momentum transfer, momentum conservation dictates that the ion recoils to the opposite direction. Mechanistically, this would occur if the electron was initially kicked in forward direction but then back-reflected at its own parent ion. Such a classical picture would suggest that the ion receives the momentum originally imparted to the electron (i.e. \mathbf{Q}) minus the final momentum \mathbf{p}_e of the electron. This expectation is verified by our measured ion momentum distributions shown in Figs. 2g-i. The ions show also a

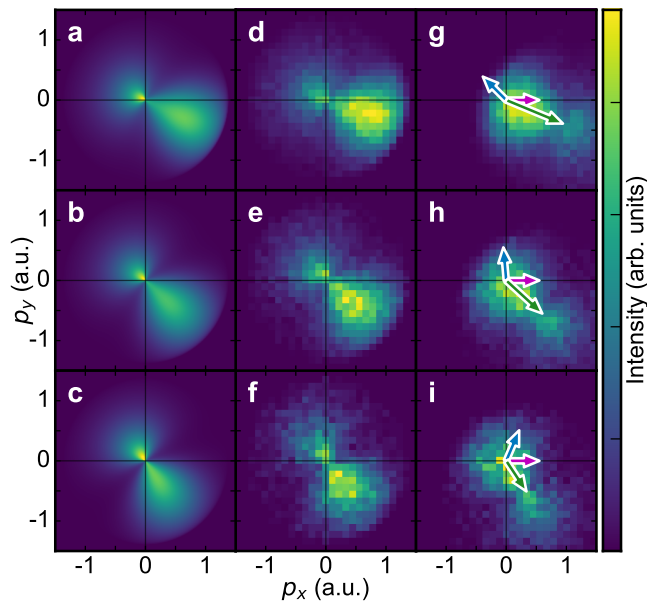


FIG. 2. **Electron and ion momentum distributions for different momentum transfer gates.** All panels use the same coordinate frame as Figs. 1b,c. **a-c**, Electron momentum distributions obtained from modelling within the A^2 approximation using approach B (see Methods). **d-f**, Electron momentum distributions measured by our experiment. **g-i**, Measured momentum distributions of the ions. From top to bottom, the rows correspond to different momentum transfers $Q = 1.0, 0.8,$ and 0.6 a.u., respectively. The arrows in the third column indicate the photon momentum configuration for each row. Here, the magenta arrows represent the momentum of the incoming photon, the blue arrows the momentum of the scattered photon, and the green arrows the momentum transfer. A movie of the electron and ion momentum distributions for different photon scattering directions is available in the supplementary materials.

bimodal momentum distribution with the main island slightly forward shifted and a minor island significantly forward shifted in momentum transfer direction, in nice agreement with the back-reflection scheme.

The observations suggest a two-step model for below-threshold Compton scattering referred to as the A^2 approximation (see Methods). The first step is the scattering of the photon at an electron being described by the Thomson cross section. This step sets the direction and magnitude of the approximate momentum transfer. The second step is the response of the electron wave function to this sudden kick which displaces the bound wave function in momentum space. This momentum-shifted electron wave function then relaxes to the electronic eigenstates of the ion where it has some overlap with its initial state and with the bound excited states. However, the fraction which overlaps with the Coulomb continuum leads to ionization and is observed experimentally. The bimodal electron momentum distribution for small momentum transfer follows naturally from such a scenario. The leading ionizing term in the Taylor expansion of the

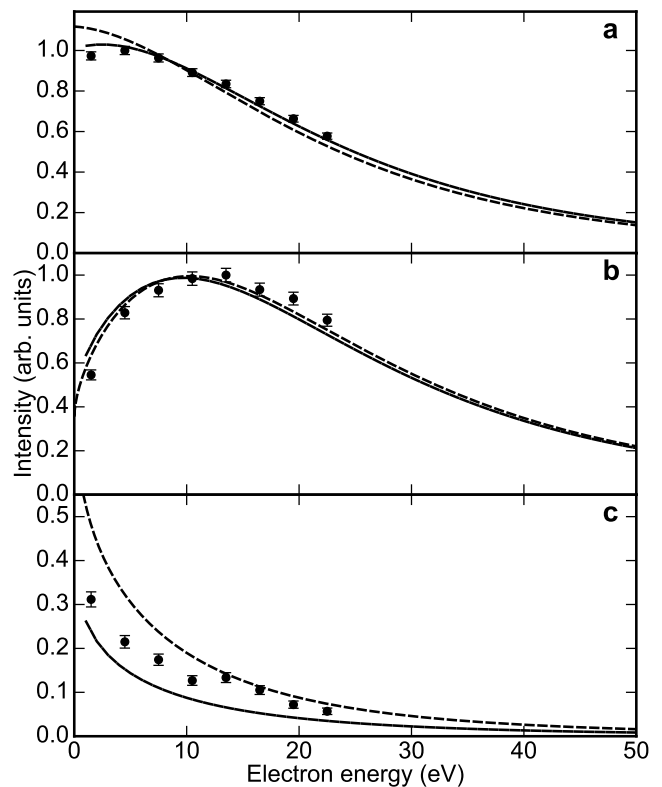


FIG. 3. **Electron energy distribution.** The scattering angle for the outgoing photon is restricted to $140 < \theta < 180$ deg in all panels. **a**, The electron energy spectrum is shown independent of the electron emission direction. **b**, The electron emission angle is restricted to forward scattering ($0 < \theta_e < 40$ deg). **c** the electron emission angle is restricted to backward scattering ($140 < \theta_e < 180$ deg). The black dots are the experimental data. The error bars are the standard statistical error. The solid lines are the theoretical results of approach A, the dashed lines the results of approach B (see Methods). The experimental data in panels **a** and **b** is normalized such that the maximum intensity is 1; the theory is normalized such that the integrals of the experimental data and the theoretical curves are equal. The normalization factors in panel **c** are identical to the ones in panel **b**, since here we depict the forward/backward direction of the same distribution.

momentum transfer operator $e^{i\mathbf{Q}\cdot\mathbf{r}_e}$ is the dipole operator with the momentum transfer replacing the direction of polarization. This dipolar contribution resembling the shape of a p orbital is the origin of the bimodal electron momentum distribution.

The observed electron momentum distributions are in excellent agreement with the prediction of the A^2 approximation shown in Fig. 2a-c. Note that these theoretical distributions are calculated without any reference to Compton scattering. What is shown is the overlap of the ground state with the continuum (altered by the momentum transfer). Exactly the same distributions are predicted for an attosecond half-cycle pulse (see Fig. 2 in [2]) and identical results are expected for a momentum transfer to the nucleus by neutron scattering [7].

Within the A^2 approximation, the magnitude of the energy transfer is determined by energy conservation. It is worth mentioning that, under the present conditions, the photon loses only a few percent of its primary energy. Thus the momentum transfer is largely a consequence of the angular deflection of the photon and not a consequence of its change in energy. This can be seen by inspecting the energy distribution of the ejected electron in Fig. 3a. The electron energy distribution peaks at zero and falls off exponentially. For electron forward emission (Fig. 3b) it peaks at 11 eV for photon back-scattering, while the backward-emitted electrons for the same conditions are much lower in energy (Fig. 3c). This also manifests itself in the fully differential cross section showing the electron angular distribution for fixed electron energy and fixed photon scattering angle of 150 ± 20 deg. These angular distributions (Fig. 4) show that the intensity in the backward directed recoil lobe compared to the intensity in the forward directed binary lobe strongly drops with increasing electron energy. The physics governing the relative strength of the binary and recoil lobe is unveiled by two sets of calculations, i.e. by comparing theoretical calculations for different initial electron wave functions and different final states. Firstly, we use a correlated two-electron wave function in the initial state with outgoing Coulomb waves with charge 1 as the final state. Secondly, we use a single-active-electron model for the initial state with a final scattering state in an effective potential (Figs. 3 and 4). We find that the binary peak is similar in all cases, the recoil peak, however, is enhanced by more than a factor of two when scattering states in an effective He^+ potential are used instead of Coulomb states. This directly supports the mechanistic argument that the recoil peak originates from back-scattering of forward-kicked electrons at the parent ion. This back-scattering is enhanced due to the increased depth of the effective potential compared to the Coulomb potential close to the origin.

In conclusion we have shown the first fully differential cross sections for Compton scattering at a gas-phase atom unveiling the mechanism of near-threshold Compton scattering. Coincidence detection of ions and electrons, as demonstrated here, paves the road to exploit Compton scattering for imaging of molecular wave functions not only averaged over the molecular axis but also in the body-fixed frame of the molecule. As has been pointed out recently, measuring the momentum transfer to the nucleus in this case will give access to the Dyson orbitals [11].

METHODS

Experimental methods. The experiment was performed at the beamline P04 of the synchrotron PETRA III, DESY in Hamburg with 40-bunch timing mode, i.e. the photon bunches were spaced 192 ns apart. A circularly polarized pink beam was used, i.e. the

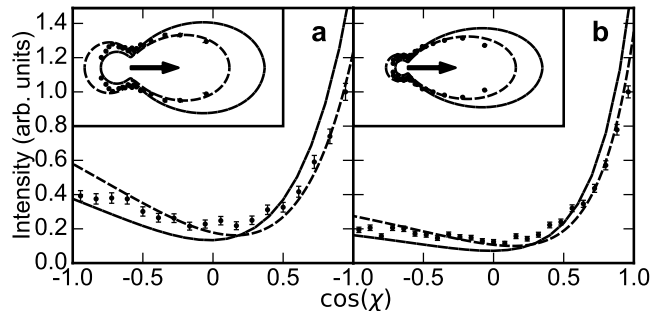


FIG. 4. **Fully differential electron angular distributions.** The photon scattering angle is $130 < \theta < 170$ deg. Displayed is the cosine of the angle χ between the outgoing electron and the momentum transfer \mathbf{Q} . **a**, The electron energy is $1.0 < E_e < 3.5$ eV. **b**, $3.5 < E_e < 8.5$ eV. The inset in the upper left is the same data in polar representation, where the arrow indicates the direction of momentum transfer. The lines and normalization are the same as in Fig. 3.

monochromator was set to zero order. To effectively remove low-energy photons from the beam, we put foil filters in the photon beam, namely 980 nm of aluminum, 144 nm of copper, and 153 nm of iron. With this setup, we suppressed photons < 100 eV by at least a factor of 10^{-9} and photons < 15 eV by at least a factor of 10^{-25} [19]. The beam was crossed at a 90 deg angle with a supersonic gas jet, expanding through a 30 μm nozzle at 30 bar driving pressure and room temperature within a COLTRIMS spectrometer. The supersonic gas jet passed two skimmers (0.3 mm diameter), hence the reaction region roughly had the size of $0.2 \times 1.0 \times 0.1$ mm^3 . The electron side of the spectrometer had 5.8 cm of acceleration. To increase resolution, an electrostatic lens and time-of-flight-focusing geometry was used for the ion side to effectively compensate for the finite size of the reaction region. The total length of the ion side was 97.4 cm. The electric field in the spectrometer was 18.3 V/cm, the magnetic field was 9.1 G. The charged particles were detected using two position-sensitive microchannel plate detectors with delay-line anodes [19].

Theoretical methods. In general, Compton scattering is a relativistic process. In the special case of an initially bound electron, this process may be described by the second-order quantum electrodynamics perturbation terms with exchange in the presence of an external classical electromagnetic field due to the residual ion (see for example [21]). In the low-energy limit of small incoming photon energy E_1 compared to the rest energy of an electron $m_e c^2$, we can apply a non-relativistic quantum-mechanical description. (In the following, we use atomic units unless stated otherwise, i.e. $e = m_e = \hbar = 1$.) The energy and momentum conservation laws are of the form

$$E_1 = E_2 + I_p + E_e + E_{\text{ion}}, \quad \mathbf{k}_1 = \mathbf{k}_2 + \mathbf{p}_e + \mathbf{p}_{\text{ion}}, \quad (1)$$

where I_p is the ionization potential, $E_e(\mathbf{p}_e)$ is the energy (momentum) of the escaped electron, $E_{\text{ion}}(\mathbf{p}_{\text{ion}})$ is the energy (momentum) of the residual ion and $E_{1/2}(\mathbf{k}_{1/2})$ are the energies (momenta) of the incoming and outgoing photons, respectively. For the given keV photon energy range, the momenta are of the order $k_i = E_i/c \sim 1$ a.u. with the speed of light $c = \alpha^{-1}$ so that the energy of the escaped electron is only a few eV. Since $M_{\text{ion}} \gg 1$, the ionic kinetic energy $E_{\text{ion}} = \mathbf{p}_{\text{ion}}^2/(2M_{\text{ion}})$ can be neglected. Hence, the photon energy is nearly unchanged and the ratio of photon energy after and before the collision is

$$t = \frac{E_2}{E_1} = 1 - \frac{I_p + E_e + E_{\text{ion}}}{E_1} \approx 1. \quad (2)$$

The transferred momentum from the photon to the atomic system is given by $\mathbf{Q} = \mathbf{k}_1 - \mathbf{k}_2 = \mathbf{p}_e + \mathbf{p}_{\text{ion}}$. The magnitude and direction of the transferred momentum \mathbf{Q} may be expressed as a function of the scattering angle θ between the incoming and outgoing photon.

Under the above kinematic conditions, the fully differential cross section (FDCS) may be written as

$$\frac{d\sigma}{dE_e d\Omega_e d\Omega_2} = r_e^2 p_e t |M|^2, \quad (3)$$

with the classical electron radius r_e and the well-known Kramers-Heisenberg-Waller matrix element (compare, for example, Refs. [21, 22]) based on the A^2 (seagull) term

$$M(\mathbf{Q}, \mathbf{p}_e) = (\mathbf{e}_1 \cdot \mathbf{e}_2) \langle \Psi_{\mathbf{p}_e}^{(-)} | \sum_{j=1}^N e^{i\mathbf{Q} \cdot \mathbf{r}_j} | \Psi_0 \rangle. \quad (4)$$

Here, $\mathbf{e}_{1/2}$ are the polarization vectors of the incoming and outgoing photons. Initially, the N electrons of the system with positions \mathbf{r}_j are in the bound state Ψ_0 . Since in the detection scheme we select singly-ionized helium ions, the final state of the electronic system is a scattering state $\Psi_{\mathbf{p}_e}^{(-)}$ with one electron in the continuum (corresponding to an asymptotic electron momentum \mathbf{p}_e) and the other electron remaining bound.

Assuming an unpolarized incoming photon beam and we do not detect the final polarization state of the outgoing photon, we additionally average over the initial polarization and sum up the probabilities corresponding to both possible orthogonal polarization states. Under these assumptions, the FDCS can be written as

$$\frac{d\sigma}{dE_e d\Omega_e d\Omega_2} = \left(\frac{d\sigma}{d\Omega_2} \right)_{\text{Th}} p_e t |M_e|^2. \quad (5)$$

The whole Compton scattering process may be divided into two steps: In the first step, the incoming photon scatters off the electronic bound-state distribution. The corresponding scattering probability is described by the Thomson formula for photons scattered off a single free electron

$$\left(\frac{d\sigma}{d\Omega_2} \right)_{\text{Th}} = \frac{1}{2} r_e^2 (1 + \cos^2 \theta). \quad (6)$$

During the short interaction with the photon, the electrons are simply “kicked” by the transferred momentum \mathbf{Q} . In the second step the “kicked”, field-free atomic system evolves in time. One part of the boosted wave function remains bound, while the other part is set free in the continuum. These escaping electrons are strongly influenced by the asymptotically Coulomb-like ionic potential so that the electronic matrix elements are given by

$$M_e(\mathbf{Q}, \mathbf{p}_e) = \langle \Psi_{\mathbf{p}_e}^{(-)} | \sum_{j=1}^N e^{i\mathbf{Q} \cdot \mathbf{r}_j} | \Psi_0 \rangle. \quad (7)$$

From the FDCS the different observables shown in the main text can be calculated.

In order to calculate the electronic matrix elements, complementary approaches have been used: The first model (approach A) describes both electrons and takes into account correlation in the ground state, but uses Coulomb waves as scattering states. In contrast, the second model (approach B) uses a single-active-electron description, but includes accurate one-electron scattering states.

Approach A: Model with correlated ground state. In the first approach, both electrons of the helium atom are explicitly treated such that the “direct” ionization of the “kicked” electron as well as the “shake-off” (i.e. ejection of the unkicked electron) are considered. In equation (7), the initial state is given by a correlated symmetric two-electron ground state $\Psi_0(\mathbf{r}_1, \mathbf{r}_2)$, obtained from [23]. To approximate the final state, the main idea is that one electron remains bound in the ionic ground state given by

$$\psi_0^{\text{He}^+}(\mathbf{r}) = \sqrt{\frac{8}{\pi}} e^{-2r} \quad (8)$$

and the free electron may be approximated by Coulomb wave functions

$$\psi_{\mathbf{p}_e}^C(\mathbf{r}) = \sqrt{\frac{e^{-\pi\zeta}}{(2\pi)^3}} \Gamma(1 - i\zeta) e^{i\mathbf{p}_e \cdot \mathbf{r}} {}_1F_1(i\zeta, 1, -ip_e r - i\mathbf{p}_e \cdot \mathbf{r}) \quad (9)$$

with $\zeta = -1/p_e$ and ${}_1F_1$ being the confluent hypergeometric function. Since the correct scattering states $\Psi_{\mathbf{p}_e}^{(-)}(\mathbf{r}_1, \mathbf{r}_2)$ have to be orthogonal to the initial bound states, the resulting symmetrized final state

$$\tilde{\Psi}_{\mathbf{p}_e}^{(-)}(\mathbf{r}_1, \mathbf{r}_2) = \frac{1}{\sqrt{2}} \left[\psi_{\mathbf{p}_e}^C(\mathbf{r}_1) \psi_0^{\text{He}^+}(\mathbf{r}_2) + \psi_{\mathbf{p}_e}^C(\mathbf{r}_2) \psi_0^{\text{He}^+}(\mathbf{r}_1) \right] \quad (10)$$

is afterwards explicitly orthogonalized with respect to the initial state Ψ_0 such that the electronic matrix elements

of equation (7) read

$$\begin{aligned} M_e(\mathbf{Q}, \mathbf{p}_e) &= \langle \Psi_{\mathbf{p}_e}^{(-)} | e^{i\mathbf{Q}\cdot\mathbf{r}_1} + e^{i\mathbf{Q}\cdot\mathbf{r}_2} | \Psi_0 \rangle \\ &= \langle \tilde{\Psi}_{\mathbf{p}_e}^{(-)} | e^{i\mathbf{Q}\cdot\mathbf{r}_1} + e^{i\mathbf{Q}\cdot\mathbf{r}_2} | \Psi_0 \rangle - \\ &\quad \langle \tilde{\Psi}_{\mathbf{p}_e}^{(-)} | \Psi_0 \rangle \langle \Psi_0 | e^{i\mathbf{Q}\cdot\mathbf{r}_1} + e^{i\mathbf{Q}\cdot\mathbf{r}_2} | \Psi_0 \rangle \quad (11) \end{aligned}$$

Approach B: Single-active-electron model. In the second approach only the “kicked” electron may escape, while the other electron stays frozen at the core. In order to model the influence of the remaining electron on the escaping electron, we use a single-active-electron effective potential [24]. This potential has an asymptotic charge of $Z = 2$ for $r \rightarrow 0$, which is screened by the second electron such that asymptotically for large r , it reaches $Z = 1$. The one-electron ground state ψ_0 and the one-electron continuum state $\psi_{\mathbf{p}_e}^{(-)}$ with incoming boundary conditions are calculated numerically via solving the radial Schrödinger equation. Hence, the electronic matrix element in equation (7) is approximated as

$$M_e(\mathbf{Q}, \mathbf{p}_e) = \sqrt{2} \langle \psi_{\mathbf{p}_e}^{(-)} | e^{i\mathbf{Q}\cdot\mathbf{r}} | \psi_0 \rangle. \quad (12)$$

This expression is calculated using a plane wave expansion of $e^{i\mathbf{Q}\cdot\mathbf{r}}$ and an expansion of the scattering states $\psi_{\mathbf{p}_e}^{(-)}$ in

terms of spherical harmonics.

ACKNOWLEDGMENTS

This work was supported by DFG and BMBF. O. Ch. acknowledges support from the Hulubei-Meshcheryakov program JINR-Romania. Calculations were performed on Central Information and Computer Complex and heterogeneous computing platform HybriLIT through supercomputer “Govorun” of JINR. Yu. P. is grateful to the Russian Foundation of Basic Research (RFBR) for the financial support under the grant No. 19-02-00014a. We are grateful to the staff of PETRA III for excellent support during the beam time.

AUTHOR CONTRIBUTION

M.K., F.T., S.G., I.V.-P., J.R., S.E., K.B., M.N.P., T.J., M.S.S., and R.D. contributed to the experimental work. S.B., N.E., S.H., O.Ch., Y.V.P., I.P.V., and M.L. contributed to theory and numerical simulations. All authors contributed to the manuscript.

-
- [1] Compton, A. H. *Secondary radiations produced by x-rays*, in Bulletin of the National Research Council, no. 20 (v. 4, pt. 2), (Published by the National Research Council of the National Academy of Sciences, Washington D.C., 1922)
- [2] Arbó, D. G., Tökési, K. & Miraglia, J. E. Atomic ionization by a sudden momentum transfer, *Nucl. Instr. Methods Phys. Res. B* **267**, 382-385 (2009)
- [3] Dürr, M. et al. Single ionization of helium by 102 eV electron impact: three dimensional images for electron emission, *J. Phys. B: At. Mol. Opt. Phys.* **39**, 4097-4111 (2006)
- [4] Ehrhardt, H., Jung, K., Knoth, G. & Schlemmer, P. Differential cross section of direct single electron impact ionization, *Z. Phys. D – Atoms, Molecules and Clusters* **1**, 3-32 (1986)
- [5] Fischer, D., Moshhammer, R., Schulz, M., Voitkiv, A. & Ullrich, J. Fully differential cross sections for the single ionization of helium by ion impact, *J. Phys. B: At. Mol. Opt. Phys.* **36**, 3555-3567 (2003)
- [6] Schulz, M et al. Three-dimensional imaging of atomic four-body processes *Nature* **422**, 48-50 (2003)
- [7] Pindzola, M. S. et al. Neutron-impact ionization of He *J. Phys. B: At. Mol. Opt. Phys.* **47**, 195202 (2014)
- [8] Bothe, W. & Geiger, H. Über das Wesen des Comptoneffekts; ein experimenteller Beitrag zur Theorie der Strahlung *Z. Phys.*, **32**, 639-663 (1925)
- [9] Bell, F., Tschentscher, Th. Schneider, J. R. & Rollason, A. J. The triple differential cross section for deep inelastic photon scattering: a $(\gamma, e\gamma')$ experiment *J. Phys. B: At. Mol. Opt. Phys.*, **24** L533-L538 (1991)
- [10] Metz, C. et al. Three-dimensional electron momentum density of aluminum by $(\gamma, e\gamma)$ spectroscopy, *Phys. Rev. B*, **59**, 10512-10520 (1999)
- [11] Hopersky, A. N., Nadolinsky, A. M., Novikov, S. A., Yavna, V. A. & Ikoeva K. Kh. X-ray-photon Compton scattering by a linear molecule *J. Phys. B: At. Mol. Opt. Phys.*, **48**, 175203 (2015)
- [12] Ullrich, J. et al. Recoil-ion and electron momentum spectroscopy: reaction-microscopes *Rep. Prog. Phys.*, **66**, 1463-1545 (2003)
- [13] Roy, S. C. & Pratt, R. H. Need for further inelastic scattering measurements at X-ray energies *Radiat. Phys. Chem.*, **69**, 193-197 (2004)
- [14] Kaliman, Z. Surić, T., Pisk, K. & Pratt, R. H. Triply differential cross section for Compton scattering *Phys. Rev. A*, **57**, 2683-2691 (1998)
- [15] Samson, J. A. R., He, Z. X., Bartlett, R. J. & Sagurton, M. Direct measurement of He^+ ions produced by Compton scattering between 2.5 and 5.5 keV *Phys. Rev. Lett.*, **72**, 3329-3331 (1994)
- [16] Spielberger, L. et al. Separation of Photoabsorption and Compton Scattering Contributions to He Single and Double Ionization *Phys. Rev. Lett.*, **74**, 4615-4618 (1995)
- [17] Dunford, R. W., Kanter, E. P., Krässig B., Southworth, S. H. & Young, L. Higher-order processes in X-ray photoionization and decay *Radiat. Phys. Chem.*, **70**, 149-172 (2004)
- [18] Kaliman, Z. & Pisk, K. Compton cross-section calculations in terms of recoil-ion momentum observables *Rad. Phys. Chem.*, **71**, 633-635 (2004)

- [19] Obtained from http://henke.lbl.gov/optical_constants/filter2.html, 10/09/2019 Data based on: Henke, B.L., Gullikson, E. M. & Davis, J. C. X-ray interactions: photoabsorbtion, scattering, transmission, and reflection at E=50-30000 eV, Z=1-92 *At. Data Nucl. Data Tables*, **54**, 181-342 (1993)
- [20] Jagutzki, O. et al. Multiple hit readout of a microchannel plate detector with a three-layer delay-line anode *IEEE Trans. Nucl. Sci.*, **49**, 2477-2483 (2002)
- [21] Akhiezer, A. I. & Berestetskii, V. B. *Quantum electrodynamics* (John Wiley & Sons, 1965)
- [22] Bergstrom Jr., P. M., Surić, T., Pisk, K. & Pratt, R. H. Compton scattering of photons from bound electrons: Full relativistic independent-particle-approximation calculations. *Phys. Rev. A*, **48**, 1134-1162 (1993)
- [23] Chuluunbaatar, O. et al. Role of the cusp conditions in electron-helium double ionization *Phys. Rev. A*, **74**, 014703 (2006)
- [24] Tong, X. M. & Lin, C. D. Empirical formula for static field ionization rates of atoms and molecules by lasers in the barrier-suppression regime. *J. Phys. B: At. Mol. Opt. Phys.*, **38**, 2593-2600 (2005)